

Revelation of Topological Surface States in Bi_2Se_3 Thin Films by *In Situ* Al Passivation

Murong Lang,^{†,||} Liang He,^{†,||,*} Faxian Xiu,[‡] Xinxin Yu,[†] Jianshi Tang,[†] Yong Wang,[§] Xufeng Kou,[†] Wanjun Jiang,[†] Alexei V. Fedorov,[⊥] and Kang L. Wang^{†,*}

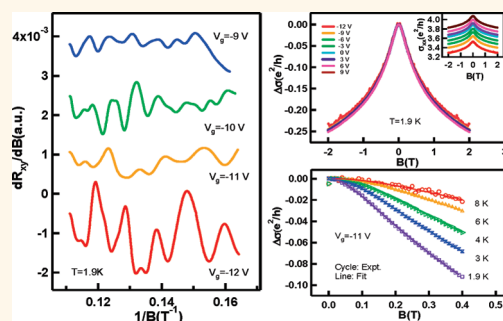
[†]Device Research Laboratory, Department of Electrical Engineering, University of California, Los Angeles, California 90095, United States, [‡]Department of Electrical and Computer Engineering, Iowa State University, Ames, Iowa 50011, United States, [§]Department of Materials Science and Engineering, Zhejiang University, Hangzhou 310027, China, and [⊥]Advanced Light Source Division, Lawrence Berkeley National Laboratory, 1 Cyclotron Road, Berkeley, California 94720, United States.

^{||}These authors contributed equally to this work.

Topological insulator (TI) is a new class of quantum matter featuring an energy gap in its bulk band structure and unique Dirac-like metallic states on the surface.^{1–5} The spins of electrons are locked perpendicular to the momentums owing to strong spin–orbit coupling, and thus backscattering is prohibited by time-reversal symmetry.^{3,6,7} Tremendous attention has been attracted to three-dimensional (3D) TIs, motivated by the discovery of quantum spin Hall effect (QSHE) in a 2D TI system—HgTe/HgCd quantum wells.^{8,9} Recently, a series of 3D TI compounds, such as $\text{Bi}_{1-x}\text{Sb}_x$, Bi_2Se_3 , Bi_2Te_3 , and Sb_2Te_3 , have been theoretically predicted and subsequently experimentally verified by angle-resolved photoemission spectroscopy (ARPES), scanning tunneling microscopy (STM), and transport measurements.^{1,2,4,5,10–14} Among all reported 3D TI materials, Bi_2Se_3 offers a large bulk band gap of 300 meV and a simple Dirac cone surface spectrum and therefore serves as a good candidate to investigate 3D TIs.⁴

To date, extensive magnetotransport experiments in Bi_2Se_3 reveal its novel surface states by angle-dependent Shubnikov–de Hass (SdH) oscillations in single crystals¹⁵ and Aharonov–Bohm interference in nanoribbons.¹⁶ Nevertheless, the degradation of surface states continuously presents a critical challenge for the further development of topological physics and practical devices. For example, Analytis *et al.*¹⁷ reported the absence of pronounced SdH oscillations after ~ 1 h atmosphere exposure. Taskin *et al.*¹⁸ found the transition of the surface states from Dirac holes to electrons after a 730 h air exposure, with the presence of SdH oscillations in both surface states. Recently, X-ray photoelectron spectroscopy (XPS) demonstrated that the rapid

ABSTRACT



Topological insulators (TIs) are extraordinary materials that possess massless, Dirac-like topological surface states in which backscattering is prohibited due to the strong spin–orbit coupling. However, there have been reports on degradation of topological surface states in ambient conditions, which presents a great challenge for probing the original topological surface states after TI materials are prepared. Here, we show that *in situ* Al passivation inside a molecular beam epitaxy (MBE) chamber could inhibit the degradation process and reveal the pristine topological surface states. Dual evidence from Shubnikov–de Hass (SdH) oscillations and weak antilocalization (WAL) effect, originated from the π Berry phase, suggests that the helically spin-polarized surface states are well preserved by the proposed *in situ* Al passivation. In contrast, we show the degradation of surface states for the unpassivated control samples, in which the 2D carrier density is increased 39.2% due to ambient n-doping, the SdH oscillations are completely absent, and a large deviation from WAL is observed.

KEYWORDS: topological insulator · aluminum passivation · thin films · Shubnikov–de Hass oscillations · weak antilocalization · surface state degradation

formation of native oxide (BiO_x) serves as the physical origin of surface degradation and environmental doping on Bi_2Se_3 .¹⁹ In addition, hydroxyl groups were also reported as surface impurities under humid ambient conditions.¹⁷ Therefore, the passivation of topological surface states is of great importance for TI study.

In our work, we present an effective approach to passivate the Bi_2Se_3 surface

* Address correspondence to wang@ee.ucla.edu, heliang@ee.ucla.edu.

Received for review September 15, 2011 and accepted December 6, 2011.

Published online December 06, 2011
10.1021/nn204239d

© 2011 American Chemical Society

with 2 nm aluminum (Al) deposition, immediately after the growth of Bi_2Se_3 thin films in MBE chamber (without breaking the ultrahigh vacuum). In order to understand the role of the Al passivation, control samples (without Al deposition) were grown under the same condition for comparison. Dual evidence from both SdH oscillations and weak antilocalization (WAL) suggests that nontrivial surface states are better revealed by *in situ* Al passivation, as it prevents native oxide (BiO_x) formation and isolates the film from ambient charges/impurities or contaminations in the subsequent fabrication process.^{17,18,20} Our results hence demonstrate that surface passivation is critical in TI surface-state-related transport studies, which could pave the way for the future practical applications, such as thermoelectric, low-noise interconnects, with possibility of extending into the low-dissipation electronics.^{21–25}

RESULTS AND DISCUSSION

Figure 1a shows a typical atomic force microscope (AFM) image of the *in situ* Al-capped 8 quintuple layer (QLs) Bi_2Se_3 film with ~ 400 nm large-scale triangle-shape terrace. Due to the naturally formed Al_2O_3 coverage, the terrace edge is not as sharp as that in the uncapped thin film, as shown in Figure 1c. Figure 1b,d displays the height profile of the red and blue lines marked in Figure 1a,c, respectively. The uniform formation of the Al_2O_3 layer is confirmed by the subnanometer roughness of the height profile in Figure 1b. For both films with and without Al capping, the height of each step is ~ 0.95 nm, which is consistent with the reported thickness of one Bi_2Se_3 QL.^{26–28}

To investigate the transport properties and explore the surface states in the passivated and unpassivated Bi_2Se_3 thin film, top-gate field-effect transistor (FET) devices with a six-terminal Hall bar geometry were fabricated, as schematically shown in Figure 2a. Standard four-point Hall measurement was carried out to eliminate the contact resistance with a constant ac current flow of 1 μA at 11.58 Hz. Figure 2b presents an optical image of the device structure. The diagonal two electrodes are top-gate electrodes, while the rest of the electrodes are connecting to the Hall bar. A zoom-in view of the Hall bar (10 μm (L) \times 20 μm (W)) is shown in the inset, with a 10 μm scale bar.

Figure 3a,b presents the temperature-dependent sheet resistances (R_s – T) of Bi_2Se_3 thin films with and without Al passivation. These two curves exhibit common features in the high-temperature range (between 250 and 35 K). First, the sheet resistances of both samples exponentially increase as temperature decreases in the temperature range from 250 to 180 K, which is similar with R_s – T curves of low bulk carrier densities ranging from 10^{16} to 10^{17} cm^{-3} that Analytis *et al.*¹⁷ reported. Second, between 35 and 180 K, the

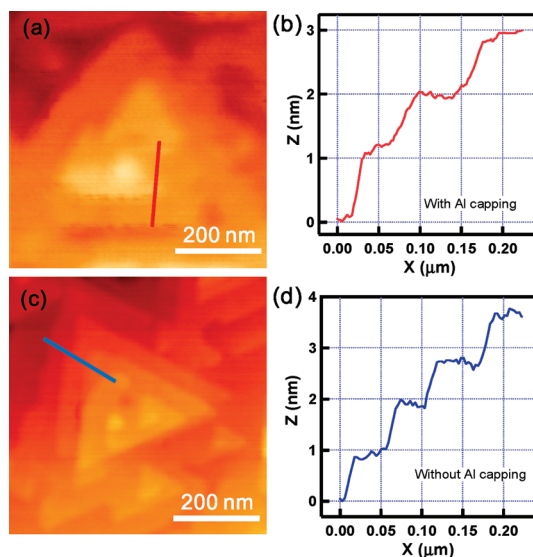


Figure 1. (a) AFM image of the *in situ* Al passivated 8 QLs Bi_2Se_3 , with ~ 400 nm large-scale triangle-shape terraces. Due to the coverage of the thin Al_2O_3 layer, the terrace edge is rounded. (b) Height profile along the solid red line marked in (a). The subnanometer roughness of the profile demonstrates the uniform formation of the thin Al_2O_3 layer. (c) AFM image of 8 QL Bi_2Se_3 without Al passivation, which shows sharp and clear terrace edge. (d) Height profile along the blue line marked in (c), showing a step size of ~ 0.95 nm.

sheet resistances decrease with the reduced temperature, implying a typical metallic behavior, in which the phonon scattering mechanism dominates.^{10,15,20} However, below 35 K, the R_s – T manifests a dramatic difference between these two samples: the device with *in situ* Al passivation displays more resistive behavior, revealing that the bulk carriers further freeze out, and therefore surface conduction is enhanced at this temperature range. However, the associated activation energy E_a cannot simply be extracted by $R \sim e^{E_a/k_B T}$ owing to the presence of multiple-channel conduction,¹³ where R is the channel resistance, k_B is the Boltzmann constant. In contrast, the sheet resistance of the unpassivated sample continuously decreases and shows a shallow local minimum at 10 K. This behavior was also observed in higher doping concentration ($n \sim 10^{19}$ cm^{-3}) Bi_2Se_3 crystals by others.^{17,29} It is noted that unpassivated devices show a dramatic reduction in sheet resistivity compared with the sample with Al passivation, which is believed to be associated with the increase of the carrier density to be discussed later.

The gate dependence of Hall carrier densities n_H in both samples at 1.9 K are extracted from $n_H = (R_H e)^{-1}$, where R_H is the Hall slope, e is the electron charge. In Figure 3c, the bulk carrier density is reduced as the gate voltage decreases, indicative of n-type bulk Bi_2Se_3 , which has been believed to be associated with Se vacancies.^{16,20,30} For the device with Al passivation, the 2D carrier density can be tuned from 5.45×10^{13} to 7.58×10^{13} cm^{-2} (with a carrier density change of

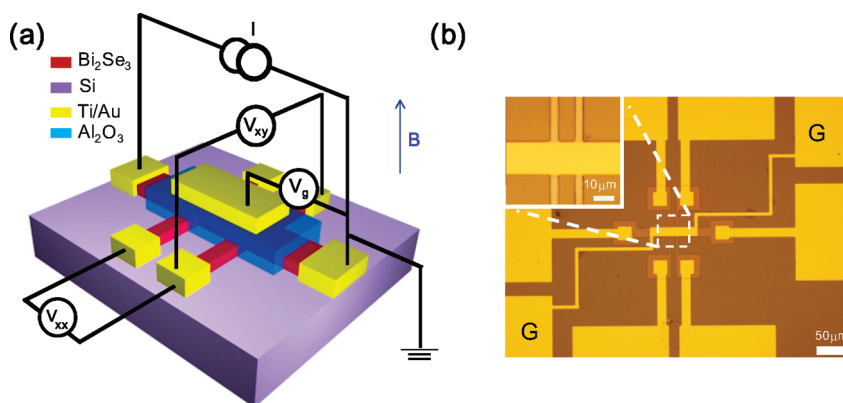


Figure 2. Top-gate FET structure and measurement setup. (a) Schematic diagram of 8 QL Bi_2Se_3 (red) on highly resistive Si(111) (purple) top-gate Hall bar device structure with measurement setup. The total thickness of Al_2O_3 (blue) is ~ 23 nm. The Al_2O_3 covers the whole substrate except the six Hall bar contact area. Here, the Al_2O_3 coverage is purposely reduced for clarity. A standard four-point measurement was carried out with constant ac current flow of $1 \mu\text{A}$. (b) Optical image of the device structure with $50 \mu\text{m}$ scale bar. Inset: zoom-in view of the optical image of the Hall bar with the size of $10 \mu\text{m}$ (L) \times $20 \mu\text{m}$ (W).

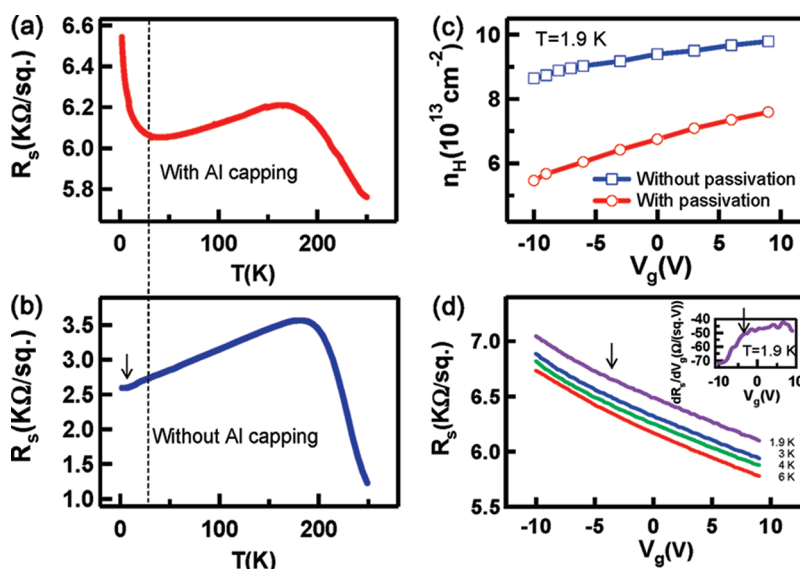


Figure 3. Transport properties in passivated and unpassivated devices. (a,b) Sheet resistances as functions of temperature, for the device with (a) and without (b) surface passivation. Two R_s - T curves (a,b) show similar behavior at high temperature but present a dramatic difference below 35 K, as indicated by the dashed line. The sheet resistance of the passivated device increases as temperature decreases, while for the unpassivated sample, the R_s continuously decreases and shows a shallow local minimum at 10 K. (c) Gate voltage dependence of 2D Hall carrier density for devices with (circles) and without (squares) Al passivation. The Hall carrier density n_H increases 39.2% at zero bias for an unpassivated sample over the passivated one. (d) Sheet resistance vs gate voltage at 1.9 , 3 , 4 , and 6 K. Arrows were used to guide the eyes, showing the sharper increase of resistance with $V_g < -4$ V. Differential resistance vs gate voltage is shown in the inset to highlight the enhancement of gating response.

39.1%), by sweeping gate voltage (V_g) from -10 to $+10$ V. In comparison, the uncapped device shows a 39.2% higher carrier concentration at zero gate bias with a relatively low gate modulation of 13.2% . This implies that the difference of the carrier concentrations arises from the unintentionally environmental n-type doping which contributes to the transport.^{17,20} As aforementioned, other surface impurities/oxides such as hydroxyl groups,¹⁷ surface native oxide (BiO_x),¹⁹ trapped charges, and impurities from ambient as well as contaminations in the fabrication process may all contribute to n-type doping. Hence, the original surface properties cannot be easily revealed if the surface is directly exposed to air or chemicals during the device

fabrication. Figure 3d presents the R_s versus V_g at various temperatures for the Al-capped device. The inset of Figure 3d shows the slope of the sheet resistance as a function of the gate voltage at 1.9 K, indicating a sharper increase in resistance beyond -4 V. This enhancement of the gating effects strongly suggests that the Fermi level is approaching the edge of the conduction band at a gate voltage of -4 V. Beyond -4 V, a large portion of bulk electrons are depleted as the Fermi level is moved into the bulk band gap.³⁰

Aiming to probe the surface electronic states for both devices, magnetotransport measurements with an out-of-plane magnetic field were conducted at low temperatures. Both gate voltage and magnetic field (B)

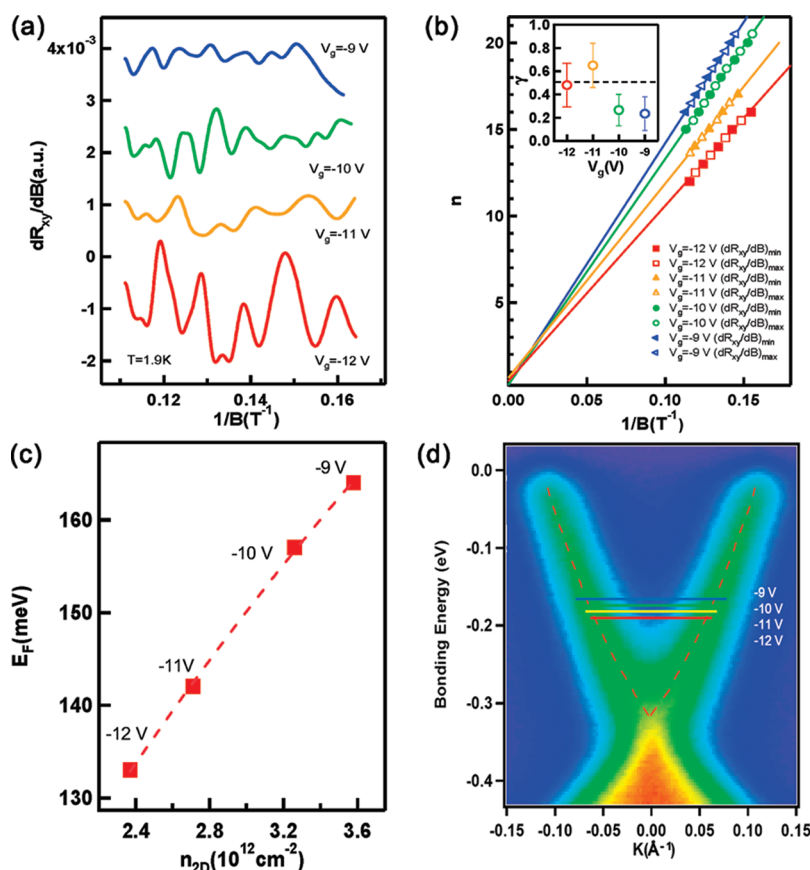


Figure 4. Gate-modulated SdH oscillations for the Al-passivated sample: (a) dR_{xy}/dB vs $1/B$ under gate voltage $V_g = -12$ to -9 V at 1.9 K, where all curves are vertically shifted for clarity. Strongly enhanced oscillations are observed when the gate bias is at -12 V. (b) Landau level fan diagram for oscillations in dR_{xy}/dB at $V_g = -12$ to -9 V. The minima (solid symbols) in dR_{xy}/dB are assigned to their indices n , while maxima (open symbols) are assigned to $n + 1/2$. The lines correspond to a linear fit to the solid and open symbols. Inset: n -axis intercept γ as a function of gate voltage. The black dashed line indicates $\gamma = 1/2$. (c) Fermi energy E_F as a function of surface 2D carrier density n_{2D} extracted from corresponding SdH oscillations. (d) ARPES intensity map of the surface states of Bi_2Se_3 thin film near the Γ point with an incident photon energy of 52 eV. The Fermi level E_F (horizontal lines) shifts toward the Dirac point as the gate voltage is decreased from -9 to -12 V.

dependences of longitudinal and transverse resistances R_{xx} and R_{xy} were recorded at various temperatures. Here, R_{xy} has a positive value at positive B field. Interestingly, in the sample with *in situ* Al capping, the magnetoresistance (MR) exhibits significantly enhanced SdH oscillations with the decrease of gate voltage (-9 to -12 V). However, SdH oscillations are completely absent in the control samples without Al capping. One possible reason is that a higher carrier concentration of the unpassivation sample suppresses the contribution from the surface state in the total conductivity, and thereby the surface property is masked.^{13,19} Another possibility could be the surface oxidation of Bi_2Se_3 in air which obscures the surface state properties due to interfacial defects or trapped charges.¹⁹

Figure 4a presents the derivative of the transverse magnetoresistance (dR_{xy}/dB) as a function of $1/B$ for the *in situ* Al-capped device. The amplitudes of the SdH oscillations are gradually enhanced with the gate bias changing from -9 to -12 V, suggesting that the bulk contribution is reduced by the external gate bias. The periodicity of such oscillations at 1.9 K is monotonically

reduced by a decreasing gate voltage from -9 to -12 V, which corresponds to the shrinking cross sectional area of Fermi surface (S_F) in momentum space as the Fermi level (E_F) approaches the Dirac point. The gate-voltage-dependent Fermi wavenumber k_F can be extracted through $\Delta(1/B) = 2e/k_F^2\hbar$ ³¹ for Dirac electrons, yielding the k_F values from 0.067 to 0.055 \AA^{-1} as gate voltage is swept from -9 to -12 V, where \hbar is Planck's constant divided by 2π .

Landau Level (LL) fan diagram is usually examined to study the Berry phase in graphene^{32,33} and surface states of TIs.^{10,17,34} Here, we assign Landau level number n ($n + 1/2$) to the minima (maxima) in the oscillations of dR_{xy}/dB shown in Figure 4a, in which n indicates $N + 1/2$ th LL, when E_F is precisely between adjacent LLs¹⁰ (see Supporting Information). On the basis of the well-known semiclassical Onsager equation, $2\pi(n + \gamma) = S_F(\hbar/eB)$,³¹ we linearly fit the SdH oscillation data in the LL fan diagram to obtain γ , where the n is the n th Landau level, and the S_F is the cross sectional area of Fermi surface; γ is directly related to the Berry phase. For a parabolic energy-momentum

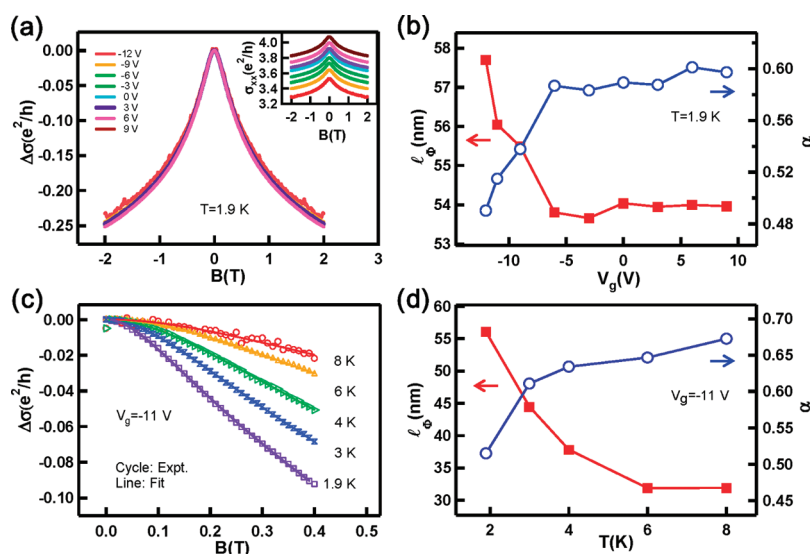


Figure 5. Gate voltage and temperature dependences of WAL for the Al-passivated sample. (a) In-plane background subtracted magnetoconductivity ($\Delta\sigma(B) = \sigma(\theta = 90^\circ, B) - \sigma(0^\circ, B)$) at 1.9 K under a set of gate biases, from -12 to 9 V with a 3 V step, showing nearly identical $\Delta\sigma(B)$ vs B curves for gate biases $V_g > -9$ V. Inset: conductivity vs magnetic field, from $V_g = -12$ V (bottom curve) to $V_g = 9$ V (top curve). (b) Fitted phase coherence length l_ϕ (solid squares) and coefficient α (open circles) from eq 1 as functions of gate voltage at 1.9 K. (c) Background subtracted magnetoconductivity at a fixed voltage $V_g = -11$ V measured at different temperatures (open circles). Lines are fitted curves by the HLN theory. (d) Fitted l_ϕ (solid squares) and α (open circles) as a function of temperature at $V_g = -11$ V, showing that the WAL effect is weakened as bulk carriers make more contributions at higher temperatures.

(E - k) band structure, γ equals 0 , corresponding to a zero Berry phase; for a linear E - k relationship, γ equals $1/2$, corresponding to a π Berry phase.^{35,36} Particularly, for TI surface states, the linear fitting of the LL fan diagram should theoretically extrapolate to $1/2$ on the n -axis. Experimentally, in Figure 4b, the LL fan diagram represents the values of $1/B$ at the minima (maxima) in dR_{xx}/dB as a function of n ($n + 1/2$) at $V_g = -12$ to -9 V at $T = 1.9$ K. The frequencies of gate-dependent SdH oscillations, given by the slopes of the linear fitting, are extracted as 98 , 112 , 135 , and 148 T under gate voltage $V_g = -12$, -11 , -10 , and -9 V, respectively. The inset shows the gate bias dependence of the intercept γ , which yields a finite Berry phase; γ is close to $1/2$ at $V_g = -12$, -11 V, while it deviates away from $1/2$ as the gate voltages increases, implying that the Fermi levels are moved from Dirac-like E - k dispersion (π Berry phase) toward quadratic E - k dispersion (zero Berry phase).³⁵ This intercept deviation was also discussed in other literature.^{17,34,35}

Figure 4c displays 2D surface carrier density n_{2D} as a function of Fermi energy E_F . The n_{2D} is effectively tuned from 3.58×10^{12} down to $2.37 \times 10^{12} \text{ cm}^{-2}$ by sweeping the gate voltage from -9 to -12 V, providing a picture for the evolution of the carrier depletion by the gating effect. Here, n_{2D} is deduced via $f = 2\pi\hbar n_{2D}/e$, where f is the above-mentioned SdH oscillation frequency obtained from the slope of the linear fitting in Figure 4b. The Fermi energy E_F corresponding to each gate voltage is given by $E_F = \hbar k_F$, which can be swept from the conduction band down to 133 meV above the Dirac point under gate bias from 0 to -12 V. Here, the Fermi velocity V_F is estimated as 3.7×10^5 m/s at $E_F \sim 140$ meV above the Dirac point,

via $V_F = (1/\hbar)(dE_F/dk_F)$ from ARPES data shown in Figure 4d, which is consistent with literature reported data^{11,17,20} (see Supporting Information). The Fermi levels at gate voltage $V_g = -9$, -10 , -11 , and -12 V are sketched (horizontal lines) in Figure 4d, which are shifted toward the Dirac point as V_g decreases.

We next explore the WAL effect for Al-capped sample, which has also been observed in other materials systems with a strong spin-orbit coupling,³⁷⁻⁴¹ such as GaAs. As shown in the inset of Figure 5a, the gate dependence of magnetoconductivity (MC) under low magnetic field was measured for the *in situ* Al-passivated device. These MC curves decrease sharply as the magnetic field increases, which is the typical response of the WAL effect.⁴² The occurrence of WAL in TIs reflects the nontrivial topology of the surface states, in which backscattering is minimized owing to the destructive interference between two time-reversed loops, arising from the π Berry phase. When a magnetic field is applied perpendicular to the film, the time reversal symmetry is broken while the possibility of backscattering increases and the WAL is suppressed.^{14,43} Through in-plane MC background subtraction, the low field MC ($\Delta\sigma(B) = \sigma(\theta = 90^\circ, B) - \sigma(0^\circ, B)$) conducted at 1.9 K is shown in Figure 5a, to exclude the 3D bulk WAL contribution (see Supporting Information), where θ is the angle between B field and the film plane. The $\Delta\sigma(B)$ versus B curves are surprisingly identical for all different gate biases except below -9 V, even though there are more than 30% changes in the Hall carrier concentration n_H (see Figure 3c). This can be attributed to the surface conduction significantly enhanced when the

bulk carrier density is sufficiently low ($V_g < -9$ V), that is, the Fermi level approaches the Dirac point.^{14,42}

In the limit of strong spin–orbit interaction in 2D electron systems, the standard Hikami–Larkin–Nagaoka (HLN) theory is often applied for weak-field conductivity variation:³⁸

$$\Delta\sigma = \frac{\alpha e^2}{2\pi^2\hbar} \left[\ln\left(\frac{\hbar}{4eBl_\phi^2}\right) - \psi\left(\frac{1}{2} + \frac{\hbar}{4eBl_\phi^2}\right) \right] \quad (1)$$

where ψ is the digamma function and the prefactor α should be equal 1/2 for the symplectic cases. One topological surface that carries a π Berry phase should give an $\alpha = 1/2$.⁴⁴ The HLN theory gives a perfect fit to all of the MC curves with various gate biases at 1.9 K shown in Figure 5a, where the phase coherence length l_ϕ and the prefactor α are two fitting parameters. The numerical fitted values α and l_ϕ as functions of gate voltages are plotted in Figure 5b. The phase coherence length l_ϕ of 57.7 nm and the prefactor α of 0.49 are obtained at -12 V and 1.9 K, indicating that there is only one surface contribution to the 2D WAL effect. This is in agreement with the recent studies on the WAL in Bi_2Se_3 ¹⁴ and Bi_2Te_3 .⁴⁵ The contribution to the WAL effect from the bottom surface seems negligible since the l_ϕ of the bottom surface is reduced due to defects caused by the lattice mismatch between Bi_2Se_3 and Si substrate.^{14,45,46} One may also notice that the l_ϕ slightly decays and α deviates from 0.5 with increasing gate voltage, which is probably due to the fact that the 2D bulk carriers contribute more to the overall conductivity of the system, with increasing gate voltage. The estimated gate dependences of the surface state parameters obtained from both SdH oscillation and WAL at $T = 1.9$ K for the Al-passivated device are summarized in Table 1.

Next, we investigate the temperature dependence of MC under a fixed gate voltage of -11 V. From the systematic trend of the MC curves in Figure 5c, it is noticed that the MC cusp at low magnetic field is broadened as temperature increases, maybe because bulk carriers are increasingly dominant at higher temperature; hence, the WAL effect arises from the weakened nontrivial surface states. This trend can also

TABLE 1. Estimated Parameters of Surface States from the SdH Oscillations and WAL for the *In Situ* Al-Passivated Sample at $T = 1.9$ K^a

V_g (V)	f_{SdH} (T)	$N_{2\text{D}}$ (10^{12} cm^{-2})	m_c (m_0)	k_F (\AA^{-1})	E_F (meV)	V_F (10^5 m/s)	l_ϕ (nm)	α
-12	98	2.37	0.170	0.055	133	3.7	57.7	0.49
-11	112	2.71	0.182	0.058	142	3.7	56.1	0.51
-10	135	3.26	0.199	0.064	157	3.7	55.8	0.52
-9	148	3.58	0.209	0.067	164	3.7	55.5	0.54

^aThe cyclotron mass is obtained from $m_c = (\hbar k_F / V_F)$, while other parameters are calculated as shown in the text.

be seen in the phase coherence length l_ϕ , which monotonically decreases from 56.1 to 31.9 nm. This similar behavior was also reported.⁴⁵ The prefactor α changes from 0.51 to 0.67 as temperature increases from 1.9 to 8 K, as presented in Figure 5d.

The fitted coefficient α agrees very well with the theoretical value at 1.9 K under $V_g = -12, -11$ V, reconfirming the existence of surface states for the Al-passivated sample. On the other hand, the device without Al passivation exhibits a large fitting deviation from the HLN theory at 1.9 K with various gate voltages applied. Therefore, it may further verify our claim that it is more challenging to probe and reveal the topological surface states in the unpassivated TI material.

CONCLUSIONS

In summary, we present the differences of transport results in MBE-grown Bi_2Se_3 samples with and without *in situ* Al passivation. Passivated 2D metallic topological surface states are better revealed with dual evidence from the SdH oscillation and WAL effects. Unpassivated samples exhibit higher carrier density, absence of quantum oscillations, as well as large deviation from WAL, suggesting that Al passivation is an effective way to preserve the topological surface states from environmental degradation. Hence our observation provides an important step toward the realization of future nanoelectronics and dissipationless spintronics devices, which may be able to take advantages of the exotic surface states in TIs.

EXPERIMENTAL METHODS

Material Growth and Sample Preparation. High-quality single-crystalline Bi_2Se_3 thin films were conducted in a PerkinElmer MBE system; MBE is a proven powerful and reliable technique to produce ultrathin TI films down to a few quintuple layers.^{28,43} The highly resistive Si(111) substrate with a resistivity $>10^4$ $\Omega \cdot \text{cm}$ was cleaned using a well-established RCA procedure before loading into the MBE chamber. High-purity Bi (99.9999%) was evaporated from conventional effusion cells at 480 °C, while Se (99.99%) was formed from a cracker cell from SVTA at 230 °C, and Si(111) substrate was kept at 250 °C during the growth. The pseudomorphic growth of Bi_2Se_3 was monitored by real-time reflection high energy electron diffraction (RHEED). After growing 8 QLs (~ 8 nm) of Bi_2Se_3 , a postannealing was

carried out at 400 °C. The thickness of 8 nm was chosen to preserve the topological surface states¹ while minimizing the contribution from the heavily doped bulk by increasing the surface-to-volume ratio. After the Bi_2Se_3 growth, a 2 nm Al was *in situ* evaporated to passivate the surface at room temperature. Al film was later naturally oxidized to form Al_2O_3 after the sample was taken out of the chamber and exposed in air, which also further serves as an initial part of the high- κ dielectric oxide stack grown by the atomic layer deposition (ALD) process. Control samples without *in situ* Al capping were grown under the same conditions. All of the samples were exposed in air for 1 day before fabrication processes began.

Device Fabrication. The MBE-grown 8 QL Bi_2Se_3 thin film was patterned into a micrometer-scale Hall bar geometry using

conventional optical photolithography and a subsequent dry etching (20 s CHF₃ etching). The 18 nm Al₂O₃ dielectric layer was conformally deposited by ALD at 150 °C to serve as the high- κ gate dielectric. Six Hall channel contacts (10 nm titanium and 90 nm gold) were defined by e-beam evaporation after dry etching the Al₂O₃ in the contact areas. The top-gate metal was defined by another step of photolithography, followed by metal deposition (Ti/Au 10 nm/90 nm) to finalize a top-gate FET fabrication process.

Characterization Methods. AFM was performed to investigate surface morphology of the Al-passivated and unpassivated Bi₂Se₃ thin film. Standard low-frequency four-probe magnetoresistance measurements were conducted in a Quantum Design Physical Properties Measurement System (PPMS) with the application of tilted magnetic fields. The temperature range is from 1.9 to 300 K, and the magnetic field is up to ± 9 T.

Acknowledgment. The authors acknowledge helpful discussions with Y. Fan, P. Upadhyaya, and technical support from L. T. Chang, X. Jiang, C. Zeng, and M. Wang from the Device Research Laboratory at UCLA. This work was in part supported by Focus Center Research Program, Center on Functional Engineered Nano Architectonics (FENA) and Defense Advanced Research Projects Agency (DARPA).

Supporting Information Available: Landau Level fan diagram, Fermi velocity V_F calculation, and angle dependence of magnetoconductivity. This material is available free of charge via the Internet at <http://pubs.acs.org>.

REFERENCES AND NOTES

- Zhang, Y.; He, K.; Chang, C.-Z.; Song, C.-L.; Wang, L.-L.; Chen, X.; Jia, J.-F.; Fang, Z.; Dai, X.; Shan, W.-Y.; *et al.* Crossover of the Three-Dimensional Topological Insulator Bi₂Se₃ to the Two-Dimensional Limit. *Nat. Phys.* **2010**, *6*, 584–588.
- Zhang, T.; Cheng, P.; Chen, X.; Jia, J.-F.; Ma, X.; He, K.; Wang, L.; Zhang, H.; Dai, X.; Fang, Z.; *et al.* Experimental Demonstration of Topological Surface States Protected by Time-Reversal Symmetry. *Phys. Rev. Lett.* **2009**, *103*, 266803.
- Qi, X.-L.; Hughes, T. L.; Zhang, S.-C. Topological Field Theory of Time-Reversal Invariant Insulators. *Phys. Rev. B* **2008**, *78*, 195424.
- Hasan, M. Z.; Kane, C. L. Colloquium: Topological Insulators. *Rev. Mod. Phys.* **2010**, *82*, 3045.
- Zhang, H.; Liu, C.-X.; Qi, X.-L.; Dai, X.; Fang, Z.; Zhang, S.-C. Topological Insulators in Bi₂Se₃, Bi₂Te₃ and Sb₂Te₃ with a Single Dirac Cone on the Surface. *Nat. Phys.* **2009**, *5*, 438–442.
- Kane, C. L.; Mele, E. J. Z₂ Topological Order and the Quantum Spin Hall Effect. *Phys. Rev. Lett.* **2005**, *95*, 146802.
- Moore, J. E.; Balents, L. Topological Invariants of Time-Reversal-Invariant Band Structures. *Phys. Rev. B* **2007**, *75*, 121306.
- König, M.; Wiedmann, S.; Brüne, C.; Roth, A.; Buhmann, H.; Molenkamp, L. W.; Qi, X.-L.; Zhang, S.-C. Quantum Spin Hall Insulator State in HgTe Quantum Wells. *Science* **2007**, *318*, 766–770.
- Bernevig, B. A.; Hughes, T. L.; Zhang, S.-C. Quantum Spin Hall Effect and Topological Phase Transition in HgTe Quantum Wells. *Science* **2006**, *314*, 1757–1761.
- Qu, D.-X.; Hor, Y. S.; Xiong, J.; Cava, R. J.; Ong, N. P. Quantum Oscillations and Hall Anomaly of Surface States in the Topological Insulator Bi₂Te₃. *Science* **2010**, *329*, 821–824.
- Xia, Y.; Qian, D.; Hsieh, D.; Wray, L.; Pal, A.; Lin, H.; Bansil, A.; Grauer, D.; Hor, Y. S.; Cava, R. J.; *et al.* Observation of a Large-Gap Topological-Insulator Class with a Single Dirac Cone on the Surface. *Nat. Phys.* **2009**, *5*, 398–402.
- Wray, L. A.; Xu, S.-Y.; Xia, Y.; Hsieh, D.; Fedorov, A. V.; Hor, Y. S.; Cava, R. J.; Bansil, A.; Lin, H.; Hasan, M. Z. A Topological Insulator Surface under Strong Coulomb, Magnetic and Disorder Perturbations. *Nat. Phys.* **2011**, *7*, 32–37.
- Xiu, F.; He, L.; Wang, Y.; Cheng, L.; Chang, L.-T.; Lang, M.; Huang, G.; Kou, X.; Zhou, Y.; Jiang, X.; *et al.* Manipulating Surface States in Topological Insulator Nanoribbons. *Nat. Nanotechnol.* **2011**, *6*, 216–221.
- Chen, J.; Qin, H. J.; Yang, F.; Liu, J.; Guan, T.; Qu, F. M.; Zhang, G. H.; Shi, J. R.; Xie, X. C.; Yang, C. L.; *et al.* Gate-Voltage Control of Chemical Potential and Weak Antilocalization in Bi₂Se₃. *Phys. Rev. Lett.* **2010**, *105*, 176602.
- Eto, K.; Ren, Z.; Taskin, A. A.; Segawa, K.; Ando, Y. Angular-Dependent Oscillations of the Magnetoresistance in Bi₂Se₃ Due to the Three-Dimensional Bulk Fermi Surface. *Phys. Rev. B* **2010**, *81*, 195309.
- Peng, H.; Lai, K.; Kong, D.; Meister, S.; Chen, Y.; Qi, X.-L.; Zhang, S.-C.; Shen, Z.-X.; Cui, Y. Aharonov-Bohm Interference in Topological Insulator Nanoribbons. *Nat. Mater.* **2010**, *9*, 225–229.
- Analytis, J. G.; McDonald, R. D.; Riggs, S. C.; Chu, J.-H.; Boebinger, G. S.; Fisher, I. R. Two-Dimensional Surface State in the Quantum Limit of a Topological Insulator. *Nat. Phys.* **2010**, *6*, 960–964.
- Taskin, A. A.; Ren, Z.; Sasaki, S.; Segawa, K.; Ando, Y. Observation of Dirac Holes and Electrons in a Topological Insulator. *Phys. Rev. Lett.* **2011**, *107*, 016801.
- Kong, D.; Cha, J. J.; Lai, K.; Peng, H.; Analytis, J. G.; Meister, S.; Chen, Y.; Zhang, H.-J.; Fisher, I. R.; Shen, Z.-X.; *et al.* Rapid Surface Oxidation as a Source of Surface Degradation Factor for Bi₂Se₃. *ACS Nano* **2011**, *5*, 4698–4703.
- Analytis, J. G.; Chu, J.-H.; Chen, Y.; Corredor, F.; McDonald, R. D.; Shen, Z. X.; Fisher, I. R. Bulk Fermi Surface Coexistence with Dirac Surface State in Bi₂Se₃: A Comparison of Photoemission and Shubnikov-de Haas Measurements. *Phys. Rev. B* **2010**, *81*, 205407.
- Teweldebrhan, D.; Goyal, V.; Balandin, A. A. Exfoliation and Characterization of Bismuth Telluride Atomic Quintuples and Quasi-Two-Dimensional Crystals. *Nano Lett.* **2010**, *10*, 1209–1218.
- Zahid, F.; Lake, R. Thermoelectric Properties of Bi₂Te₃ Atomic Quintuple Thin Films. *Appl. Phys. Lett.* **2010**, *97*, 212102.
- Goyal, V. Mechanically-Exfoliated Stacks of Thin Films of Bi₂Te₃ Topological Insulators with Enhanced Thermoelectric Performance. *Appl. Phys. Lett.* **2010**, *97*, 133117.
- Hossain, M. Z.; Romyantsev, S. L.; Shahil, K. M. F.; Teweldebrhan, D.; Shur, M.; Balandin, A. A. Low-Frequency Current Fluctuations in “Graphene-like” Exfoliated Thin-Films of Bismuth Selenide Topological Insulators. *ACS Nano* **2011**, *5*, 2657–2663.
- Shahil, K. M. Crystal Symmetry Breaking in Few-Quintuple Bi₂Te₃ Films: Applications in Nanometrology of Topological Insulators. *Appl. Phys. Lett.* **2010**, *96*, 153103.
- Lind, H.; Lidin, S.; Häussermann, U. Structure and Bonding Properties of (Bi₂Se₃)_m(Bi₂)_n Stacks by First-Principles Density Functional Theory. *Phys. Rev. B* **2005**, *72*, 184101.
- Kou, X. F.; He, L.; Xiu, F. X.; Lang, M. R.; Liao, Z. M.; Wang, Y.; Fedorov, A. V.; Yu, X. X.; Tang, J. S.; Huang, G.; *et al.* Epitaxial Growth of High Mobility Bi₂Se₃ Thin Films on CdS. *Appl. Phys. Lett.* **2011**, *98*, 242102.
- He, L.; Xiu, F.; Wang, Y.; Fedorov, A. V.; Huang, G.; Kou, X.; Lang, M.; Beyermann, W. P.; Zou, J.; Wang, K. L. Epitaxial Growth of Bi₂Se₃ Topological Insulator Thin Films on Si (111). *J. Appl. Phys.* **2011**, *109*, 103702.
- Butch, N. P.; Kirshenbaum, K.; Syers, P.; Sushkov, A. B.; Jenkins, G. S.; Drew, H. D.; Paglione, J. Strong Surface Scattering in Ultrahigh-Mobility Bi₂Se₃ Topological Insulator Crystals. *Phys. Rev. B* **2010**, *81*, 241301.
- Kong, D.; Dang, W.; Cha, J. J.; Li, H.; Meister, S.; Peng, H.; Liu, Z.; Cui, Y. Few-Layer Nanoplates of Bi₂Se₃ and Bi₂Te₃ with Highly Tunable Chemical Potential. *Nano Lett.* **2010**, *10*, 2245–2250.
- Onsager, L. Interpretation of the de Haas-van Alphen Effect. *Philos. Mag.* **1952**, *43*, 1006–1008.
- Zhang, Y.; Tan, Y.-W.; Stormer, H. L.; Kim, P. Experimental Observation of the Quantum Hall Effect and Berry's Phase in Graphene. *Nature* **2005**, *438*, 201–204.
- Novoselov, K. S.; Geim, A. K.; Morozov, S. V.; Jiang, D.; Katsnelson, M. I.; Grigorieva, I. V.; Dubonos, S. V.; Firsov, A. A. Two-Dimensional Gas of Massless Dirac Fermions in Graphene. *Nature* **2005**, *438*, 197–200.
- Ren, Z.; Taskin, A. A.; Sasaki, S.; Segawa, K.; Ando, Y. Large Bulk Resistivity and Surface Quantum Oscillations in the

- Topological Insulator $\text{Bi}_2\text{Te}_2\text{Se}$. *Phys. Rev. B* **2010**, *82*, 241306.
35. Taskin, A. A.; Ando, Y. Berry Phase of Nonideal Dirac Fermions in Topological Insulators. *Phys. Rev. B* **2011**, *84*, 035301.
 36. Mikitik, G. P.; Sharlai, Y. V. Manifestation of Berry's Phase in Metal Physics. *Phys. Rev. Lett.* **1999**, *82*, 2147–2150.
 37. Bergmann, G. Weak Localization in Thin Films: A Time-of-Flight Experiment with Conduction Electrons. *Phys. Rep.* **1984**, *107*, 1–58.
 38. Hikami, S.; Larkin, A. I.; Nagaoka, Y. Spin–Orbit Interaction of Magnetoresistance in the Two Dimensional Random System. *Prog. Theor. Phys.* **1980**, *63*, 707–710.
 39. Dresselhaus, P. D.; Papavassiliou, C. M. A.; Wheeler, R. G.; Sacks, R. N. Observation of Spin Precession in GaAs Inversion Layers Using Antilocalization. *Phys. Rev. Lett.* **1992**, *68*, 106.
 40. Chen, G. L.; Han, J.; Huang, T. T.; Datta, S.; Janes, D. B. Observation of the Interfacial-Field-Induced Weak Antilocalization in InAs Quantum Structures. *Phys. Rev. B* **1993**, *47*, 4084.
 41. Koga, T.; Nitta, J.; Akazaki, T.; Takayanagi, H. Rashba Spin–Orbit Coupling Probed by the Weak Antilocalization Analysis in InAlAs/InGaAs/InAlAs Quantum Wells as a Function of Quantum Well Asymmetry. *Phys. Rev. Lett.* **2002**, *89*, 046801.
 42. Kim, Y. S.; Brahlek, M.; Bansal, N.; Edrey, E.; Kapilevich, G. A.; Iida, K.; Tanimura, M.; Horibe, Y.; Cheong, S.-W.; Oh, S. Thickness-Dependent Bulk Properties and Weak Antilocalization Effect in Topological Insulator Bi_2Se_3 . *Phys. Rev. B* **2011**, *84*, 073109.
 43. Liu, M.; Chang, C.-Z.; Zhang, Z.; Zhang, Y.; Ruan, W.; He, K.; Wang, L.-l.; Chen, X.; Jia, J.-F.; Zhang, S.-C.; *et al.* Electron Interaction-Driven Insulating Ground State in Bi_2Se_3 Topological Insulators in the Two-Dimensional Limit. *Phys. Rev. B* **2011**, *83*, 165440.
 44. Lu, H.-Z.; Shen, S.-Q. Weak Localization of Bulk Channels in Topological Insulator Thin Films. *Phys. Rev. B* **2011**, *84*, 125138.
 45. He, H.-T.; Wang, G.; Zhang, T.; Sou, I.-K.; Wong, G. K. L.; Wang, J.-N.; Lu, H.-Z.; Shen, S.-Q.; Zhang, F.-C. Impurity Effect on Weak Antilocalization in the Topological Insulator Bi_2Te_3 . *Phys. Rev. Lett.* **2011**, *106*, 166805.
 46. Chen, J.; He, X. Y.; Wu, K. H.; Ji, Z. Q.; Lu, L.; Shi, J. R.; Smet, J. H.; Li, Y. Q. Tunable Surface Conductivity in Bi_2Se_3 Revealed in Diffusive Electron Transport. *Phys. Rev. B* **2011**, *83*, 241304.